Supplement of Atmos. Chem. Phys., 25, 18187–18208, 2025
https://doi.org/10.5194/acp-25-18187-2025-supplement

Supplement of

Sea breeze-driven daytime vertical distributions of air pollutants and photochemical implications in an island environment

Bohai Li et al.

Correspondence to: Shanshan Wang (shanshanwang@fudan.edu.cn)

S1. Calculation of detection limits for differential slant range column concentrations of species with different pitch angles

DSCD Detection Limit (DDL) of Differential Slant Column Density (DSCD) is the minimum concentration or column concentration value that can be reliably detected when measuring a specific gas by differential slant column concentration (DSCD). The following equation was used to estimate the DSCD DDL for NO_2, HCHO and CHOCHO at α elevation angle (Peters et al., 2012):

$$\mathrm{DDL}(\alpha) = \frac{2\mathrm{RMS}_{\mathrm{mean}}(\alpha)}{\sigma_{\mathrm{max}}}$$

where DDL is the minimum DSCD that can be obtained from MAX-DOAS measurements; $\mathrm{RMS}_{\mathrm{mean}}$ is the mean RMS, and σ_{max} is the maximum value of the corresponding species transect. Also, we calculated the minimum value of DSCD at different elevation angles ($\mathrm{DSCD}_{\mathrm{min}}$) and the residual percentage (RP) of values above the DDL, which are listed along with the DDL in Table S2.

S2. Detailed process and function explanation of Sea Breeze's objective recognition algorithm

According to Figure S4, the specific functions and meanings of the filters in each module are as follows:

Module 1: In the absence of geostrophic wind, the onshore flow in a pure sea breeze (SB) circulation is easily identifiable. However, when the SB interacts with synoptic-scale circulation, its velocity and direction are significantly influenced by the background wind. Therefore, identifying SB days requires first screening for large-scale background circulation patterns conducive to SB formation. To mitigate the impact of rapidly changing background fields, the following criteria are applied: (1) the 700 hPa wind direction (WD) must vary by less than 90° within 12 hours, and the wind speed (WS) must vary by less than 6 m s^{-1} within the same period (Filter 1); (2) the WS at 700 hPa at 08:00 must be less than 11 m s^{-1} to eliminate the influence of strong background fields (Filter 2).

Module 2: The three channels of Module 2 have different functions. Channel 1 selects a special SBDs where the SB is coming in almost all day, so the time window defined for it is from local sunrise (LSR, 06:00) to midnight (24:00) (Filter 3-1). In Channel 1, the following criteria are applied: (1) the WD must consistently fall within 213°–74° for at least 14 consecutive hours (Filter 4-1), and (2) The WS at a given moment t (WS_t) must increase by more than 15% compared to the previous hour ($\Delta WS_t \geq 15\%\ WS_{t-1}$), followed by a sustained upward trend for at least 3 hours (Filter 5-1). The time satisfying these conditions is recorded as the SB onset time (O_{time}). During the period from the moment before local sunset (LSS, 19:00) to the next sunrise, which is prone to SB front dissipation (Filter 6), the SB cessation time (C_{time}) is identified when the WD at a given moment t (WD_t) shifts to 74°–213° or the WS decreases by more than 15% (Filter 7-1).

If Channel 1 criteria are not met, the algorithm proceeds to Channel 2. Here, to ensure the selection of SB events within the complete diurnal cycle, the period between local sunrise (LSR, 06:00) and the moment before local sunset (LSS, 18:00) is defined as the window of potential SB occurrence (Filter 3-2). A sudden WD shift ($\Delta WD_t \geq 30°$) followed by at least 3 hours of onshore wind ($WD \geq 213°$ or $\leq 74°$) is considered a key feature of SB establishment (Filter 4-2). The time of this shift is recorded as O_{time}. After onset, WS typically exhibits a sustained increase. The maximum WS (WS_{max}) between O_{time} and LSS is identified, and the acceleration (a) must be ≥ 0.1 m $(s\ h)^{-1}$ during this period (Filter 5-2). Similar to Channel 1, cessation is constrained to the sunset-to-sunrise period (Filter 6) and is identified when $WS_{\mathrm{max}} \leq 1.5$ m s^{-1} or WD_t shifts to 74°-213° (Filter 7-2). WS_{max} is used instead of WS_t because it more reliably represents SB cessation, as WS_t rarely drops below 1.5 m s^{-1}, which could lead to premature detection of cessation. WD_t serves as a secondary criterion since the reversal from onshore to offshore flow does not always occur at the end of the diurnal cycle.

If Channel 2 criteria are not met, the algorithm proceeds to Channel 3. A time window from 10:00 to 19:00 is defined (Filter 3-3). Typically, relative humidity (RH) increases significantly with the onset of a marine air mass. To distinguish non-sea breeze days (NSBDs) from sea breeze days (SBDs) filtered by Channels 1 and 2, abnormal RH fluctuations are rejected. An abnormal fluctuation is identified when the rate of change of RH at a certain moment t ($R_{\Delta RH(t)}$) is greater than 0, and the rate of change of RH at the previous moment of t ($R_{\Delta RH(t-1)}$) and at least one subsequent moment ($R_{\Delta RH(t+n+1)}$, n = 1, 2, 3⋯⋯) are both less than 0

(Filter 8). If maximum value of the rate of change (R_{max}) is less than or equal to 8% from the t to t+n (n = 1, 2, 3……), the fluctuation is considered minor and ignored (Filter 9), and NSBDs are successfully identified.

Module 3: The pressure field is crucial as it provides the driving force for the development of low-level SBs. This thermal wave is induced by temperature variations within the atmospheric boundary layer. Figure S5 illustrates the average atmospheric tide during the study period, revealing a regular diurnal cycle. The maximum surface pressure (SP) at night occurred at 23:00 (998.54 mb) and the minimum at 05:00 (996.85 mb), while the maximum SP during the day occurred at 10:00 (998.35 mb) and the minimum at 17:00 (995.79 mb). The semi-diurnal pressure wave is calculated as: Atide = (P10+P23) − (P5-P17) (Azorin-Molina et al., 2011). The following criteria were adopted for screening the barometric field:

1、$C_{pres} - Min_{pres} \geq 0\ mb$, where C_{pres} is the SP at SB cessation and Min_{pres} is the minimum SP measured between onset (O_{time}) and cessation (C_{time}) (Filter 10).

2、$Atide_{daily} - Atide_{general} \geq -5\ mb$, where $Atide_{daily}$ and $Atide_{general}$ represent the semi-daily baroclinic wave for each SB day selected in the first two modules and for the entire 3-month study period, respectively. Dates with maximum negative values (less than -5) will be excluded as they indicate a significant change in weather (Filter 11)

Module 4: ΔT provides local forcing for the development of SBs. It is therefore important to ensure that the local daily maximum temperature (AirT2m) exceeds the average daily temperature (SST) of the surrounding sea area (Filter 12).

S3. k-means clustering

K-means clustering, an unsupervised machine learning algorithm, effectively groups similar data points without prior labels. To investigate the influence of different summertime meteorological patterns on O_3 concentration and formation from a diurnal perspective, we applied this method to cluster the 24-h O_3 concentration time series from nearby DongPo School monitoring station (DPS) on NSBDs and SBDs (including those selected by Channel 1). The optimal number of clusters (k) was determined using the Davies-Bouldin Index (DBI), which evaluates clustering performance by assigning lower values to well-separated clusters (Davies and Bouldin, 1979). Among k values ranging from 2 to 8, k = 5 was selected as it yielded the lowest DBI (Fig. S13).

Table S1. Spectral analysis configurations for inversion of O_4, NO_2, HCHO and CHOCHO slant column concentrations in QDOAS and the absorption cross sections considered.

Parameter	Cross section	UV		VIS	
		O_4	HCHO	NO_2	CHOCHO
Fitting spectral range		338-370nm	324.5-359nm	415-450nm	420-460nm
Wavelength calibration		Based on a high-resolution solar reference spectrum			
Fraunhofer reference		Sequential zenith spectrum			
NO_2	Vandaele et al. (1998), 220, 298 K	√	√	√	√
O_3	Serdyuchenko et al. (2014), 223 K, 243K	√	√	√ (only 223 K)	√ (only 223 K)
O_4	Thalman and Volkamer (2013), 293 K	√	√	√	√
HCHO	Meller and Moortgat (2000), 298 K	√	√	×	×
CHOCHO	Volkamer et al. (2005), 296 K	×	×	√	√
SO_2	Bogumil et al. (2003), 293 K	×	√	×	×
H_2O	Rothman et al. (2010), 296 K	×	×	√	√
BrO	Fleischmann et al. (2004), 223 K	√	√	×	×
Ring	Ring spectrum calculated from DOASIS (Kraus, 2006) and additional ring multiplied by λ^{-4} (Wagner et al., 2009)	√	√	√	√
Polynomial degree		Order 3	Order 5	Order 3	Order 5
Intensity offset		Constant	Order1	Constant	Constant

Table S2. Summary of DSCD DDLs, DSCD minima ($DSCD_{min}$), and residual percentages (RP) after filtering results below NO_2, HCHO, and CHOCHO DDLs.

Eva (°)	NO_2			HCHO			CHOCHO		
	DDL (molec cm^{-2})	$DSCD_{min}$ (molec cm^{-2})	RP (%)	DDL (molec cm^{-2})	$DSCD_{min}$ (molec cm^{-2})	RP (%)	DDL (molec cm^{-2})	$DSCD_{min}$ (molec cm^{-2})	RP (%)
2	9.80E+14	3.40E+15	100	7.21E+15	3.15E+15	99.1	7.82E+14	4.58E+14	99.5
3	9.50E+14	1.74E+15	100	7.15E+15	2.65E+15	98.9	7.47E+14	3.59E+14	99.2
4	9.14E+14	2.64E+15	100	7.09E+15	3.01E+15	99.1	7.17E+14	3.22E+14	99.0
6	8.36E+14	1.95E+15	100	6.97E+15	2.93E+15	99.4	6.60E+14	2.80E+14	98.7
8	7.73E+14	1.93E+15	100	6.88E+15	3.00E+15	99.0	6.13E+14	3.12E+14	98.6
10	7.17E+14	1.73E+15	100	6.79E+15	3.63E+15	99.2	5.77E+14	2.60E+14	98.2
15	6.09E+14	1.33E+15	100	6.57E+15	3.08E+15	98.4	5.13E+14	2.59E+14	96.9
20	5.33E+14	1.16E+15	100	6.07E+15	2.89E+15	99.1	4.70E+14	2.07E+14	94.5
30	4.39E+14	9.47E+14	100	5.33E+15	2.92E+15	99.0	4.18E+14	1.74E+14	87.7

Table S3. Frequency and specific dates of non-sea breeze days (NSBDs), sea breeze days (SBDs) and typhoon days (TDs) selected by the identification algorithm for the summer of 2024 at Fuke village (FK).

Weather pattern	frequency	Channel	The time of occurrence	note
NSBDs	32	Channel 3	2024.06.02-2024.06.04; 2024.06.11-2024.06.13; 2024.06.15-2024.06.20; 2024.06.29-2024.06.30; 2024.07.01-2024.07.02; 2024.07.09-2024.07.10; 2024.07.12; 2024.08.06-2024.08.11; 2024.08.18; 2024.08.20-2024.08.23; 2024.08.27	Instruments were not observed on some dates due to power outages, maintenance, etc.
SBDs	31	Channel 1	2024.06.01; 2024.06.06; 2024.08.15-2024.08.16	Includes 2024.07.09-2024.07.13;2024.07.22; 2024.08.30-2024.08.31
		Channel 2	2024.06.05; 2024.06.08-2024.06.10; 2024.06.21; 2024.06.23; 2024.06.25-2024.06.28; 2024.07.03-2024.07.08; 2024.07.13; 2024.07.17-2024.07.20; 2024.08.04-2024.08.05; 2024.08.24-2024. 08.26; 2024.08.31	
TDs	7		2024.07.21-2024.07.27	

Table S4. Summary of meteorological variables and their applications in the three datasets used in this study.

Type	Time scale	coordinate range	Meteorological variables
ERA5 Hourly Data on Single Levels	June 1, 2024 to August 31, 2024	18.04-20.18°N, 108.28-111.2°E	Sea surface temperature Downward UV radiation at the surface
ERA5 Hourly Data on Pressure Levels		19.53°N, 109.14°E	700hpa to 1000hpa Temperature 700hpa to 1000hpa Relative humidity 700hpa to 1000hpa vertical velocity
ERA5-Land Hourly Data			2m temperature 2m dew temperature 10m u-component of wind 10m v-component of wind Surface pressure Total precipitation

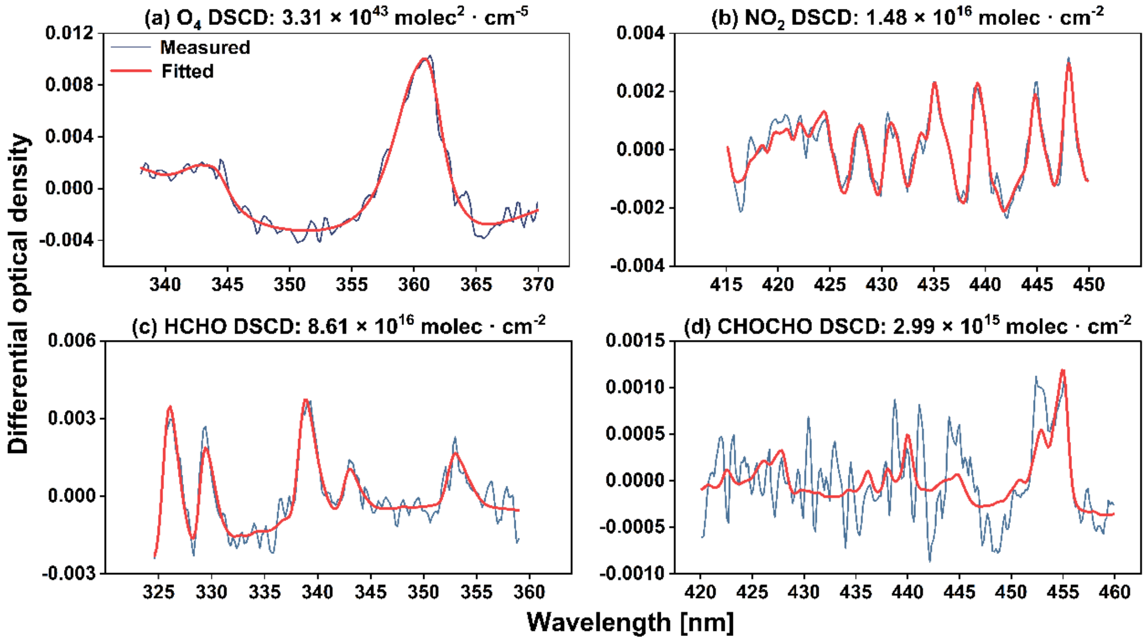

Figure S1. Examples of typical differential optical absorption spectra (DOAS) spectral fits for (a) O_4, (b) NO_2, (c) HCHO, and (d) CHOCHO. Taken on June 15, 2024 at 11:21 local time with an elevation angle of 4°. The fitted differential slant column densities (DSCDs) are given in the individual subpanels.

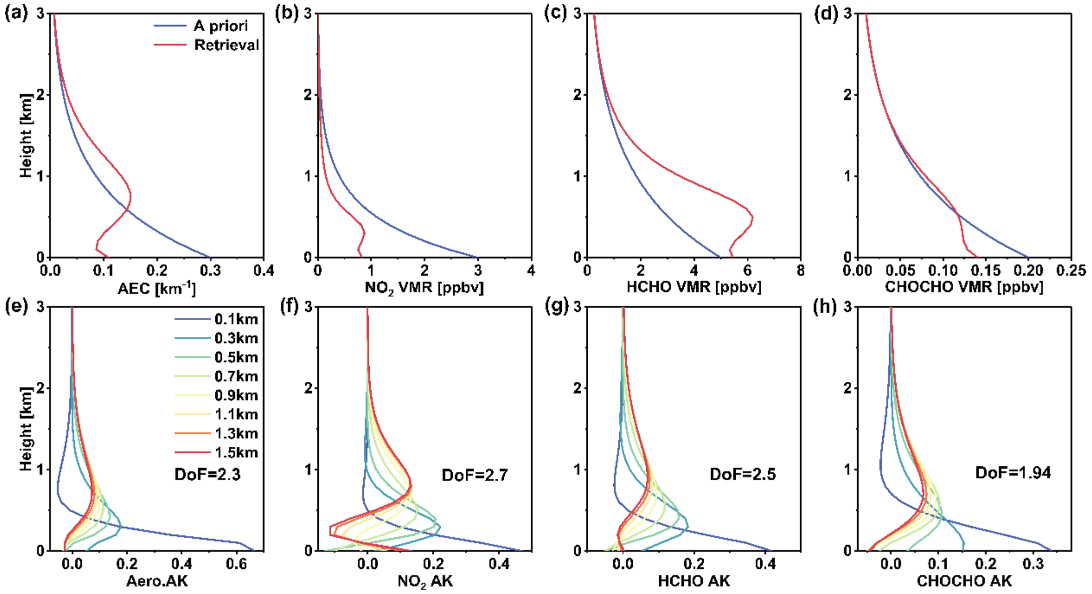

Figure S2. Examples of a priori profile and vertical profile inversions for aerosol extinction, NO_2, HCHO, and CHOCHO on June 15, 2024, at about 11:45 local time, along with degree-of-freedom information on the profile inversion signals. The upper panel shows (a) aerosol extinction, (b) NO_2 and (c) HCHO and (d) CHOCHO profiles. The lower panel shows the averaging kernel with information about the degrees of freedom of the signals retrieved by the (e) aerosol extinction, (f) NO_2, (g) HCHO, and (h) CHOCHO contours.

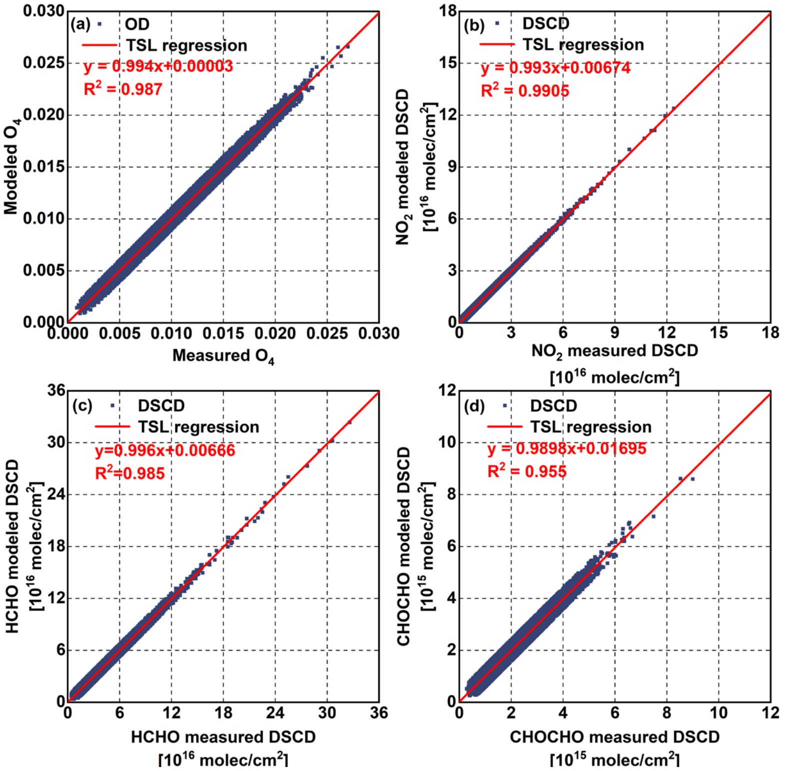

Figure S3. Scatter plots of measured DSCDs (ODs) against modelled DSCDs (ODs) during the whole measurement period for retrievals of (a) aerosols, (b) NO_2, (c) HCHO, and (d) CHOCHO. The squares of the correlation coefficients (R^2) and the slopes derived from the linear regressions (red lines) are given in each subplot.

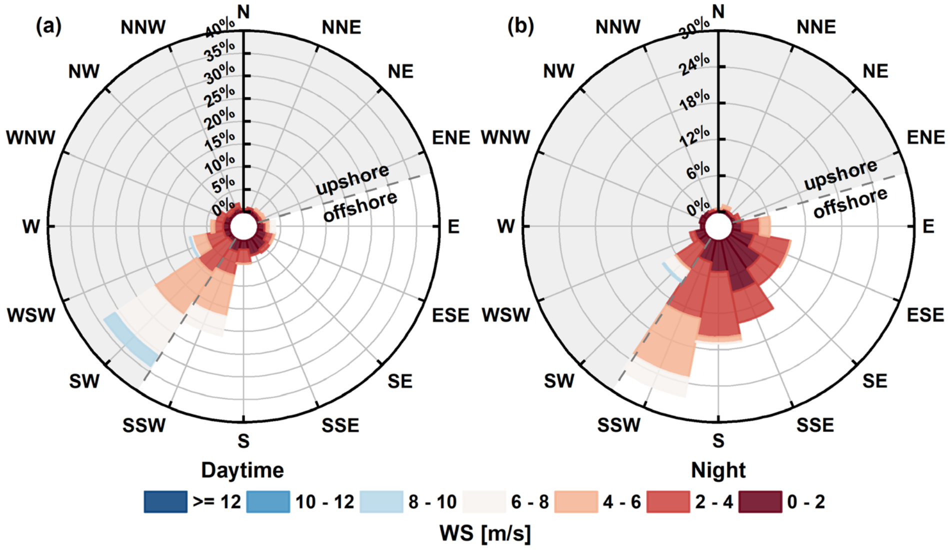

Figure S4. Wind rose plots during the observation period for daytime (a) and night (b). The gray shaded area indicates onshore WD, and the gray dashed line represents the coastline. WD is plotted in polar coordinates with percentage frequency indicated by concentric circles.

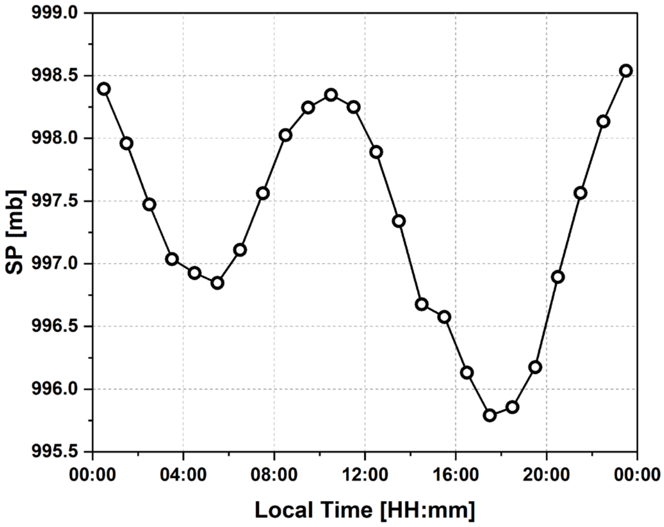

Figure S5. Daily cycle of local hourly mean surface pressure (SP) perturbations over the 3-month study period (2024.0601-2024.08.31).

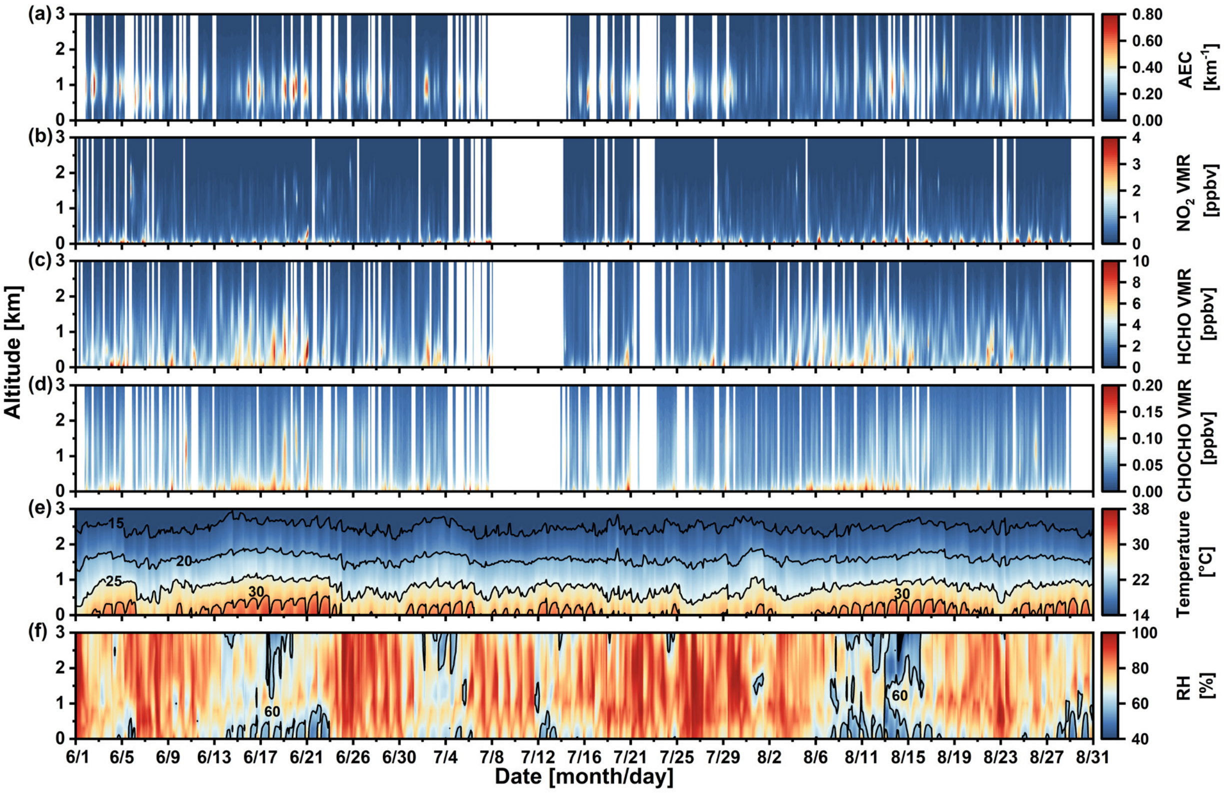

Figure S6. Time series of (a) aerosol, (b) NO$_2$, (c) HCHO, and (d) CHOCHO vertical profiles derived from MAX-DOAS measurements, along with vertical profiles of (e) temperature and (f) relative humidity (RH) obtained from ERA5 data. Data gaps occurred due to power outages, instrument malfunctions, quality control exclusions, and short-term maintenance.

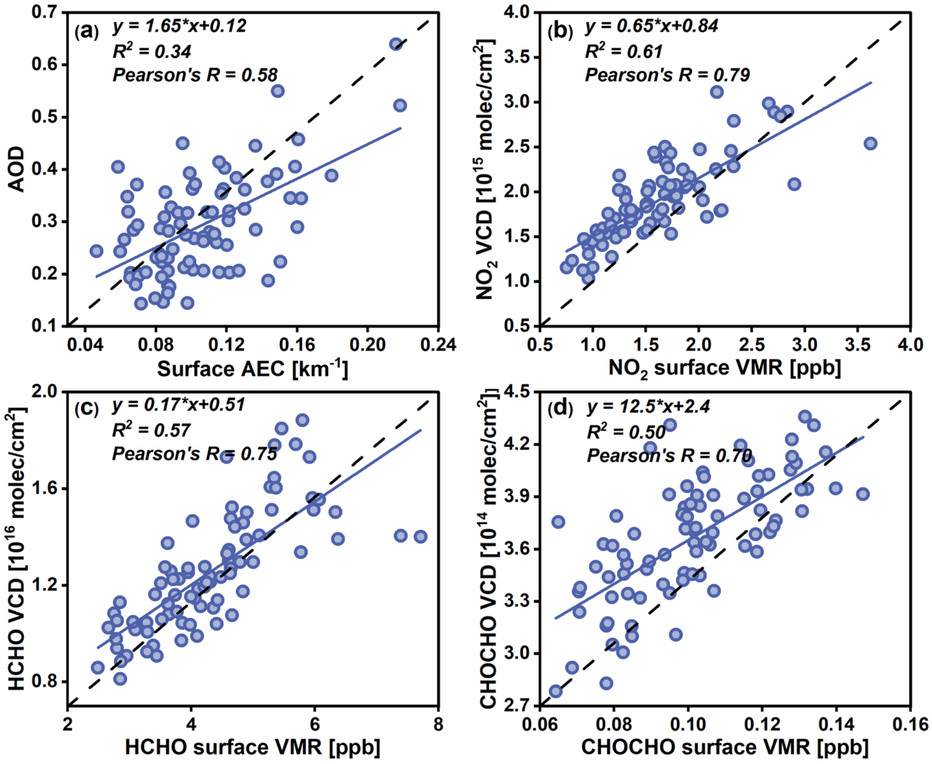

Figure S7. Correlations between surface and column integrated concentrations of (a) aerosol; (b) NO_2; (c) HCHO; and (d) CHOCHO during the observation period. The black dashed line represents the scaled reference line, while the blue solid line indicates the linear regression line. The regression equation, coefficient of determination (R^2), and Pearson correlation coefficient are shown in the upper-left corner of each panel.

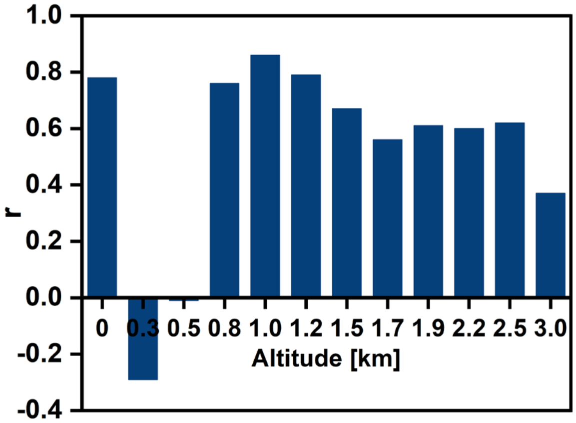

Figure S8. Pearson correlation coefficients (r) between AEC and RH at each altitude during the same time.

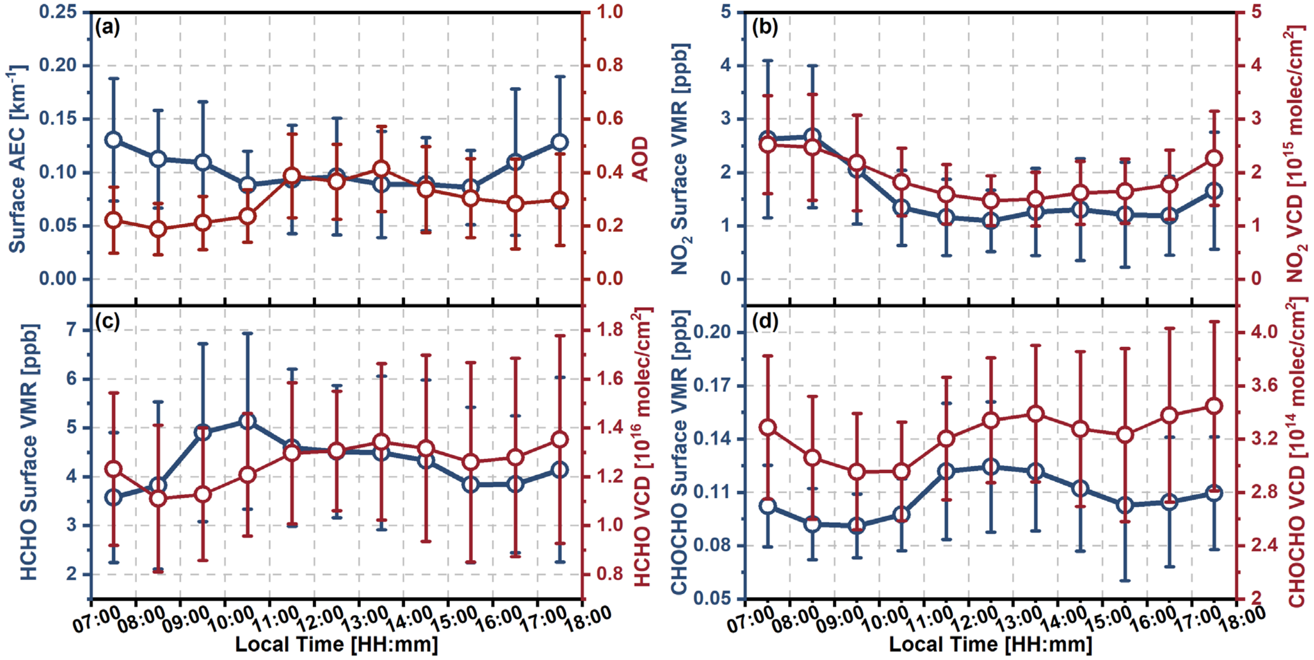

Figure S9. Diurnal cycles of the (a) surface AEC and AOD, along with surface VMRs and VCDs of (b) NO₂, (c) HCHO and (d) CHOCHO.

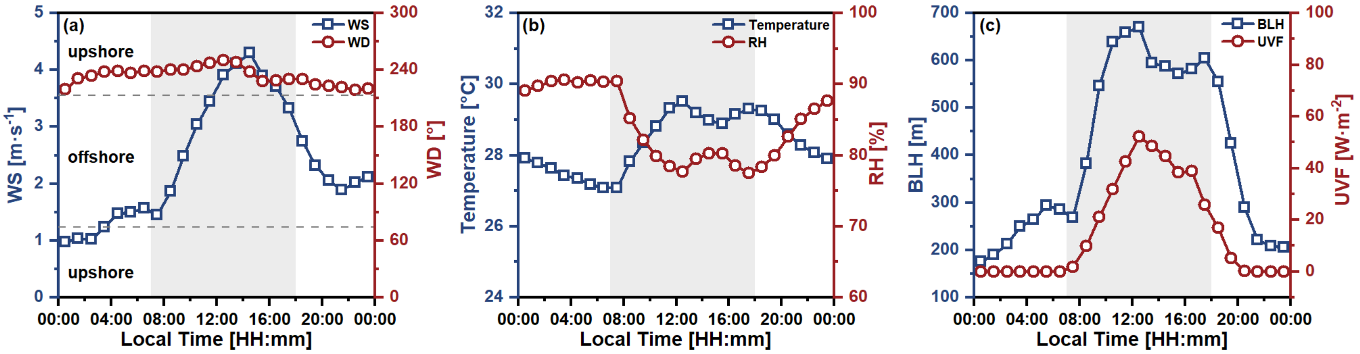

Figure S10. Mean daily cycles of WS, WD, temperature, RH, BLH, and UV radiation flux (UVF) for the SB selected for channel 1.

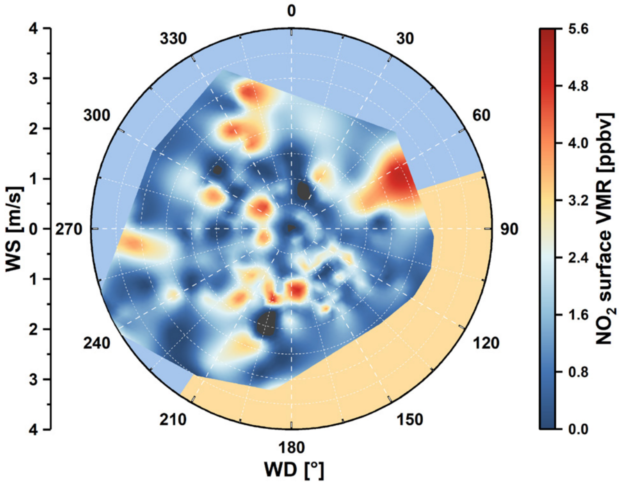

Figure S11. Wind rose diagram for NO_2 on SBDs. Blue areas represent onshore winds and yellow areas represent offshore winds.

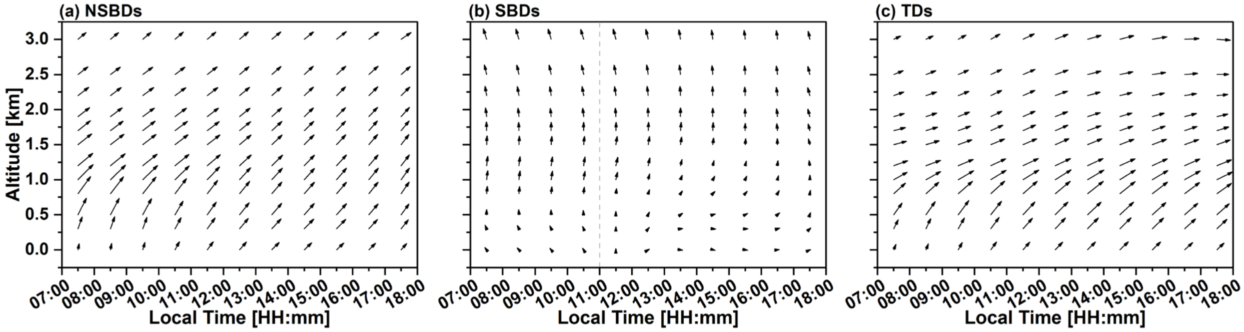

Figure S12. Wind profiles for different air current patterns. The lengths of the arrows indicate the magnitude of the wind speeds and they are subjected to the same scaling factor on the three air current patterns (ACPs). The gray dotted line refers to the O_{time} of the SB.

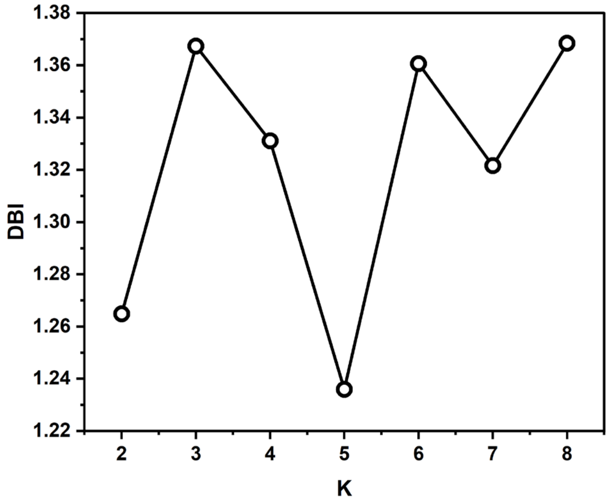

Figure S13. Characterization of the variation of the Davies-Bouldin Index (DBI) with the number of clusters (k).

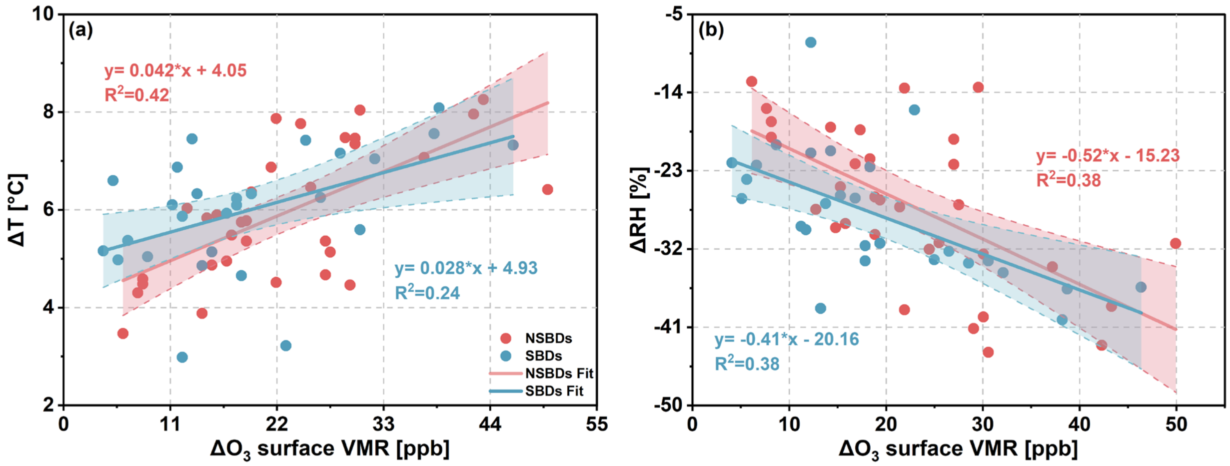

Figure S14. Correlation of net ozone increment (ΔO_3) with the change of (a) temperature (ΔT) and (b) RH (ΔRH) for each day of the NSBDs and SBDs, respectively.

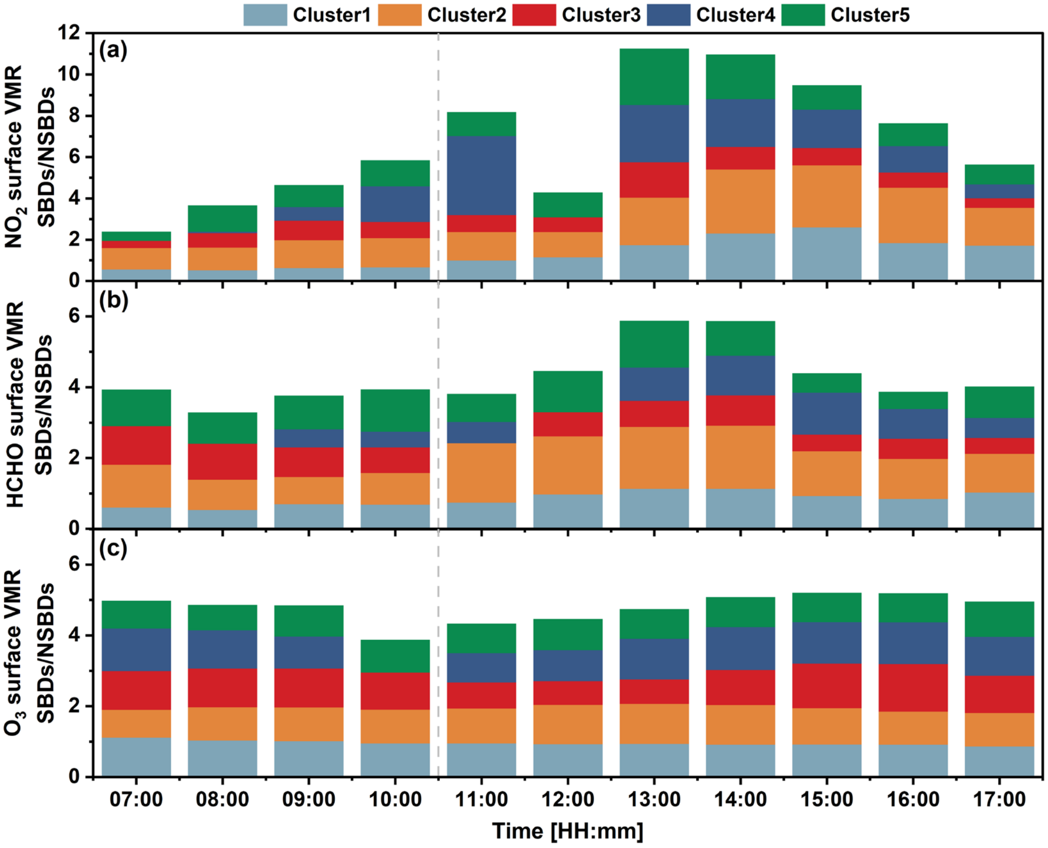

Figure S15. Daily cycling of cumulative ratios (R_{SN}) of (a) NO_2, (b) HCHO and (c) CHOCHO surface VMR between SBDs and NSBDs in five clusters. The gray dotted line refers to the O_{time} of the SB. Cluster 4 has no data for some moments of the SBDs.

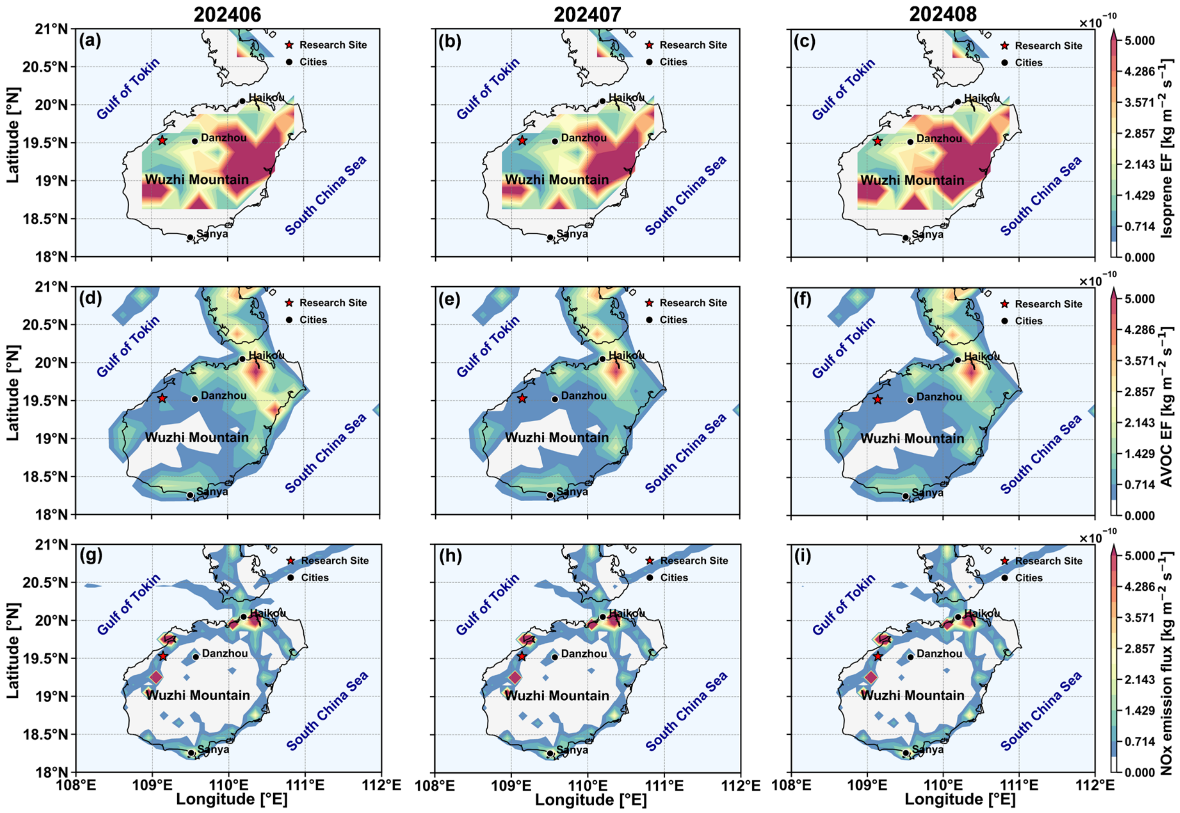

Figure S16. Monthly distributions of (a–c) isoprene, (d–f) anthropogenic VOCs (AVOCs), and (g–i) anthropogenic NO$_x$ emission fluxes (EF) over Hainan Island for June–August 2024.

References:

Azorin-Molina, C., Tijm, S., and Chen, D.: Development of selection algorithms and databases for sea breeze studies, Theor. Appl. Climatol., 106, 531-546, https://doi.org/10.1007/s00704-011-0454-4, 2011.

Bogumil, K., Orphal, J., Homann, T., Voigt, S., Spietz, P., Fleischmann, O. C., Vogel, A., Hartmann, M., Kromminga, H., Bovensmann, H., Frerick, J., and Burrows, J. P.: Measurements of molecular absorption spectra with the SCIAMACHY pre-flight model: instrument characterization and reference data for atmospheric remote-sensing in the 230–2380 nm region, J. Photochem. Photobiol., A, 157, 167-184, https://doi.org/10.1016/S1010-6030(03)00062-5, 2003.

Davies, D. L. and Bouldin, D. W.: A Cluster Separation Measure, IEEE Trans. Pattern Anal. Mach. Intell., PAMI-1, 224-227, https://doi.org/10.1109/TPAMI.1979.4766909, 1979.

Fleischmann, O. C., Hartmann, M., Burrows, J. P., and Orphal, J.: New ultraviolet absorption cross-sections of BrO at atmospheric temperatures measured by time-windowing Fourier transform spectroscopy, J. Photochem. Photobiol., A, 168, 117-132, https://doi.org/10.1016/j.jphotochem.2004.03.026, 2004.

Kraus, S.: DOASIS: a framework design for DOAS, 182, 2006.

Meller, R. and Moortgat, G. K.: Temperature dependence of the absorption cross sections of formaldehyde between 223 and 323 K in the wavelength range 225–375 nm, J. Geophys. Res.: Atmos., 105, 7089-7101, https://doi.org/10.1029/1999JD901074, 2000.

Peters, E., Wittrock, F., Großmann, K., Frieß, U., Richter, A., and Burrows, J. P.: Formaldehyde and nitrogen dioxide over the remote western Pacific Ocean: SCIAMACHY and GOME-2 validation using ship-based MAX-DOAS observations, Atmos. Chem. Phys., 12, 11179-11197, https://doi.org/10.5194/acp-12-11179-2012, 2012.

Rothman, L. S., Gordon, I. E., Barber, R. J., Dothe, H., Gamache, R. R., Goldman, A., Perevalov, V. I., Tashkun, S. A., and Tennyson, J.: HITEMP, the high-temperature molecular spectroscopic database, J. Quant. Spectrosc. Radiat. Transfer, 111, 2139-2150, https://doi.org/10.1016/j.jqsrt.2010.05.001, 2010.

Serdyuchenko, A., Gorshelev, V., Weber, M., Chehade, W., and Burrows, J. P.: High spectral resolution ozone absorption cross-sections – Part 2: Temperature dependence, Atmos. Meas. Tech., 7, 625-636, https://doi.org/10.5194/amt-7-625-2014, 2014.

Thalman, R. and Volkamer, R.: Temperature dependent absorption cross-sections of O_2–O_2 collision pairs between 340 and 630 nm and at atmospherically relevant pressure, Physical Chemistry Chemical Physics, 15, 15371-15381, https://doi.org/10.1039/C3CP50968K, 2013.

Vandaele, A. C., Hermans, C., Simon, P. C., Carleer, M., Colin, R., Fally, S., Mérienne, M. F., Jenouvrier, A., and Coquart, B.: Measurements of the NO_2 absorption cross-section from 42000 cm^{-1} to 10000 cm^{-1} (238–1000 nm) at 220 K and 294 K, J. Quant. Spectrosc. Radiat. Transfer, 59, 171-184, https://doi.org/10.1016/S0022-4073(97)00168-4, 1998.

Volkamer, R., Molina, L. T., Molina, M. J., Shirley, T., and Brune, W. H.: DOAS measurement of glyoxal as an indicator for fast VOC chemistry in urban air, Geophys. Res. Lett., 32, https://doi.org/10.1029/2005GL022616, 2005.

Wagner, T., Beirle, S., and Deutschmann, T.: Three-dimensional simulation of the Ring effect in observations of scattered sun light using Monte Carlo radiative transfer models, Atmos. Meas. Tech., 2, 113-124, https://doi.org/10.5194/amt-2-113-2009, 2009.